PCCP

PAPER

View Article Online
View Journal | View Issue

Cite this: *Phys. Chem. Chem. Phys.*, 2023, **25**, 494

Tribochemically driven dehydrogenation of undoped sodium alanate under room temperature†‡

Esmeralda Muñoz-Cortés, [a] Olga L. Ibryaeva, [b] Miguel Manso Silvan, [c] Borja Zabala, [d] Eduardo Flores, [e] Almudena Gutierrez, [f] Jose Ramon Ares [a] and Roman Nevshupa *[f]

Received 7th October 2022,
Accepted 30th November 2022

DOI: 10.1039/d2cp04681d

rsc.li/pccp

An application of mechanical energy was explored as a new non-thermal method to drive H_2 emission from undoped sodium alanate at room temperature. It was found that mild rubbing of $NaAlH_4$ pellets under vacuum led to intensive and almost instantaneous gas emission. The dominating species in the emitted gases was H_2 (>99%). Traces of mono- and polyalanes, $NaAlH_4$ vapours, CO_2 and other non-identified gases were registered. H_2 emission involved several first-order processes, whose characteristic time constants ranged widely from 0.6 to 465 s. None of the dehydrogenation reactions could be connected to either the thermal effect of friction or the direct coupling of mechanical forces to the energy landscape of chemical reactions. In turn, it was suggested that the tribochemical reactions can be triggered by plastic deformation and shearing. A linked diffusion-wear model of $NaAlH_4$ triboinduced dehydrogenation, which consistently explains all empirical findings, was put forward.

1 Introduction

Alkali metal alanates are a class of materials containing anionic metal complexes $[AlH_4]^-$ and alkali metal cations (Li, Na, K). Among them, sodium alanate ($NaAlH_4$) has the most attractive combination of thermodynamic properties and capacity for hydrogen storage (5.6 wt% H_2) which makes it a promising candidate for hydrogen energy applications.[1] For alkaline alanates, the hydrogen release usually occurs in three consecutive thermally activated reactions ((R1)–(R3)) being (R1) and (R2) the most interesting for typical applications:

$$NaAlH_4 \rightarrow \frac{1}{3}Na_3AlH_6 + \frac{2}{3}Al + H_2; \quad T = 200 - 220^\circ \quad (R1)$$

$$\frac{1}{3}Na_3AlH_6 \rightarrow NaH + \frac{1}{3}Al + \frac{1}{2}H_2; \quad T = 240 - 260^\circ \quad (R2)$$

$$NaH + Al \rightarrow NaAl + \frac{1}{2}H_2; \quad (R3)$$

Even though both $NaAlH_4$ and Na_3AlH_6 have suitable reaction enthalpies (−37 and −47 kJ mol^{-1} H_2, respectively), the high activation barrier (~120 kJ mol^{-1} H_2 for $NaAlH_4$)[1] poses a serious limitation for the use of alanates as rechargeable hydrogen storage material.[2] The barriers in (R1) and (R2) are mainly associated with a series of mass-transfer and phase-transition reactions, which involve the nucleation of new phases, phase segregation, and diffusion of vacancies and defects. The reversibility of hydrogenation of alanates was improved by adding titanium-based catalyst,[3] which lowers the activation energies in (R1) and (R2) by 50 and 20 kJ mol^{-1} H_2, respectively.

A large variety of alternative strategies pursuing the further enhancement of de- and hydrogenation performance of alkali alanates has been explored so far. Such strategies employ doping with selected transition metals,[4,5] adding metal chlorides, fluorides and oxides, decreasing the crystal size by mechanical milling,[6,7] confining within nanopores and nanostructures,[8–11]

[a] *Department of Physics of Materials, Universidad Autónoma de Madrid, Spain*
[b] *Department of Applied Mathematics and Computer Science, South Ural State University, Chelyabinsk, Russia*
[c] *Department of Applied Physics, Nicolás Cabrera Institute and Centre for Microanalysis of Materials, Universidad Autónoma de Madrid, Spain*
[d] *Tribology & Materials Unit, Fundación Tekniler, Eibar, Spain*
[e] *Departamento de Física Aplicada, Centro de Investigación y de Estudios Avanzados (CINVESTAV), 97310, Mérida, Mexico*
[f] *Eduardo Torroja Institute of Construction Sciences (IETCC), CSIC, Madrid, Spain. E-mail: r.nevshupa@csic.es; Tel: +34 91103 5746*

† Open access research data are available at Digital CSIC DOI: **https://doi.org/10.20350/digitalCSIC/14811**.

‡ Electronic supplementary information (ESI) available: Structural characterization of $NaAlH_4$ powder, details of the experimental setup and procedure for mechanically stimulated gas emission mass spectrometry, results of FTIR analysis, details of the pencil matrix method, analysis of the reaction order of "trail" emission, and analysis of the hypotheses about the mechanisms of hydrogen emission. See DOI: **https://doi.org/10.1039/d2cp04681d**

and supporting on 2D carbon allotropes[12] among others. Despite enormous efforts made during the last two decades, the physical-chemical mechanisms of $NaAlH_4$ dehydrogenation/hydrogenation remain under debate, and the corresponding hydrogen storage technology has not yet reached the readiness level sufficient for its commercial use. In this context, exploring different approaches and less conventional methods can be useful to extend the horizons of research and, in the end, find an efficient and effective solution to the problem of solid-state hydrogen storage.

One such approach is based on the employment of non-thermal energies such as mechanical, photo, and microwave.[13] In the past our group explored the effectiveness of mechanical energy in driving dehydrogenation of MgH_2 being one of the most stable hydrides.[14] The results were striking since a high degree of dehydrogenation (>70%) was achieved by mild rubbing under vacuum at room temperature. These results manifest the peculiar role that tribophysical[15,16] and tribochemical[17] processes may have for driving dehydrogenation of hydrides at room temperature though they seem to contradict other findings such as the lack of any considerable signs of MgH_2 dehydrogenation when it is ball-milled under an inert atmosphere[18] or the existence of an opposite reaction of ball-milling assisted synthesis of MgH_2 from Mg under H_2.[19] Rubbing is playing the key role since it produces intensive shearing of surface layers under relatively low loads and well-defined load-speed conditions. This is distinct from a conventional ball-milling process, which involves a larger contribution of impact and larger dispersion of local load-speed conditions. Also, in comparison with ball milling, mild friction causes a notably smaller increase in surface temperature.[16] In our previous study, the instant "flash" increase of temperature on local spots of MgH_2 hardly exceeded 320 K, which was far below the temperature required for its thermally activated dehydrogenation (≥570 K). Apparently, a vacuum environment is another important factor since it promotes the escape of H_2 from the material subjected to mechanical deformation and decreases the rate of the opposite reaction. These observations are in line with the broader tribochemical perspective,[14,16,20,21] in which most mechanochemical reactions conducted under mild rubbing conditions are considered non-thermally driven, while the activation mechanisms are related to bond tension and twisting, reduction of potential barriers, interactions with crystal defects and dislocations, electric charge generation, and exo-electron emission among other processes.[22–24]

From the standpoint of mechanochemical phenomenology, there are certain similarities between alkali alanates and MgH_2: both MgH_2 and $NaAlH_4$ are stable under mechanical milling[25] and can be formed by mechanochemical synthesis from metal precursors under a H_2 atmosphere.[26,27] Here, the question arises of whether $NaAlH_4$ is as susceptible to tribochemical dehydrogenation as MgH_2 is under similar conditions.

The study presented in this work was aimed at exploring, for the first time, the non-thermal dehydrogenation processes for sodium alanate. The dehydrogenation reactions were studied on a micrometre scale using localized rubbing under ultrahigh vacuum. Mechanically Stimulated Gas Emission Mass-Spectrometry (MSGE-MS) was used to determine the kinetic parameters of dehydrogenation as well as the composition and emission behaviour of trace gases, in *operando* conditions, in accordance with a previously developed original method.[28,29] It was complemented by structural, morphological and surface analyses, and modelling to unveil how elemental chemical reactions and gas transport in the bulk and across the surface are coupled with plastic deformation and fracture in the complex hydride.

2 Materials and procedure

$NaAlH_4$ powder (>93%) was purchased from Sigma Aldrich and kept in a glove box under Ar in a sealed flask. X-Ray diffraction with Cu K_α (λ = 0.15418 nm) radiation was employed for the structural characterization of $NaAlH_4$ (See Fig. S1 in ESI‡).

To assess the thermal stability of $NaAlH_4$ Temperature-Programmed Desorption Mass Spectrometry (TPD-MS) with alumina crucibles was used. An alumina crucible was used instead of a Pt one to avoid the possible catalytic effect of Pt on the decomposition of $NaAlH_4$. A portion of $NaAlH_4$ powder was placed into an alumina crucible in a glove box under Ar atmosphere (<1 ppm H_2O, <1 ppm O_2), and then the alumina crucible was transferred to the TPD-MS system, where it was set into another Pt crucible. During the transfer, the sample was briefly exposed to the atmospheric air (about 5 min). The test was carried out under an Ar flux of 50 mL s^{-1} and a heating rate of 5 °C min^{-1}.

For the mechanochemical test, cylindrical pellets, 13 mm in diameter and 1 mm thick, were fabricated by compacting $NaAlH_4$ powder in a die under a uni-axial pressure of 370 MPa. The pellets were subjected to reciprocating rubbing under high vacuum (10^{-7} mbar range) using an alumina sphere, 3 mm in diameter. A specially designed friction cell with nearly zero own gas emission was used.[30] The motion frequency was 1 Hz. One motion cycle consisted of one forward and one backward stroke, each of which lasted for about 40 ms. The indenter stood still for around 50 ms after the forward stroke and 870 ms after the backward one. The stroke length was l_a = 7 mm, the mean sliding speed was V_s = 0.18 m s^{-1} and the normal load was in the range 0.22–0.88 N. The total and partial gas pressures were measured in the experimental vacuum chamber, where the pellets were rubbed, using an ionization Bayard-Alpert type vacuum gauge and a quadrupole mass-spectrometer, correspondingly. To quantify minute gas emission rates (<1 nmol s^{-1}) the experimental chamber was connected to a gas-expansion one through a diaphragm, whose conductance under molecular gas flow was carefully measured.[30] The schematic drawing of the experimental system is shown in Fig. S2 in ESI‡ while the detailed description of the system and the procedure for measuring MSGE can be found elsewhere.[30,31] Before starting the experiments, the chamber was pumped out for at least 48 hours to achieve stable background pressure (the rate of change of low-pass filtered pressure signal ≤10^{-11} mbar s^{-1}). The gas emission was evaluated from the pressure time series during the

mechanical action and benchmarked against the stable background. Spectral analysis of emission oscillation was carried out using Fast Fourier Transform with Hamming window. The gas composition and the emission rates were determined using a previously developed statistical matrix method.[32–34] If not stated otherwise, each test was carried out on a pristine surface zone.

The coefficient of friction on the pellets was measured in a separate experiment using an original ultrahigh vacuum tribometer Ca[3]UHV with a reciprocating motion configuration.[31] An alumina ball, 3 mm in diameter, was used as an indenter. The normal loads were 2–10 N, the stroke length was 3 mm and the mean sliding velocity was 0.147 mm s^{-1}.

The mechanically affected zones (MAZ) were characterized using μ-FTIR spectrometry, μ-Raman confocal spectroscopy (incident laser wavelength λ = 532 nm and power 5.6 mW) and Scanning Electron Microscopy (Hitachi S-3000N). Ultra-microindentation was carried out using a diamond Berkovich indenter. Indentations were performed with a Shimadzu DUH-200 dynamic ultra-microhardness tester (0.02 mN load and 0.005 mm depth resolutions) applying 16 loading-unloading tests at each load on different areas of the pellet. Indentations with maximal loads of 1, 2 and 5 mN were used to estimate the hardness and elastic modulus of sodium alanate according to the model described by Pharr and Oliver, which includes elastic recovery corrections to the microscopic estimations of plastic deformation area.[35] All the results were benchmarked against the measurements on the pristine zones of the same pellets.

3 Results and discussion

3.1 Thermal desorption

Hydrogen emission during a temperature ramp is shown in Fig. 1. The H_2 emission (H_2^+ m/z = 2) agrees the common three-stage behaviour according to reactions (R1)–(R3).[36] The signal with m/z = 41, which showed strong linear correlation with H_2 emission, was assigned to argonium (ArH^+). Argonium can be usually formed by low-energy collisions of hydrogen and argon ions and/or molecules in an ionization chamber of a mass-spectrometer.[37] Apart from H_2, emission of trace gases, which were only partially identified, was registered in the temperature range 180–240 °C (a blue highlighted region in Fig. 1), *i.e.* before the main H_2 emission events. The emission of trace gases did not correlate with H_2. We concluded that the trace gases shouldn't be related to thermal reactions (R1)–(R3). Further details about trace gases can be found in ESI.‡

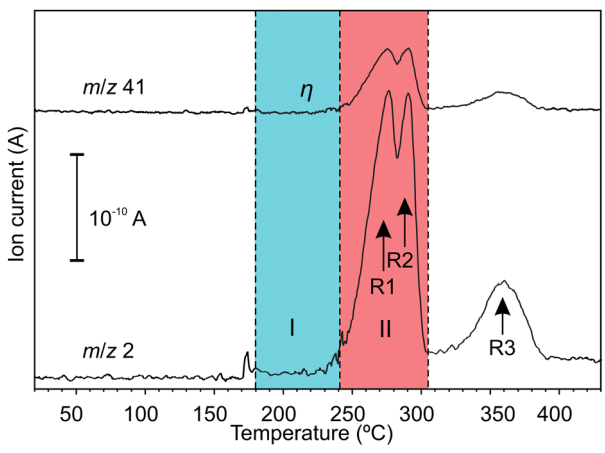

Fig. 1 Mass-spectrometric signals with increasing temperature; region I corresponds to the initial stage after melting (T = 180–240 °C); region II corresponds to the main stage at which H_2 emission occurs *via* reactions (R1) and (R2) (T = 240–305 °C).

3.2 MSGE-MS

3.2.1 Gas composition and emission rates. The mean composition of the gases emitted during rubbing is shown in Fig. 2. Hydrogen accounted for more than 99% of the total emission rate. The most striking results were that tribo-induced dehydrogenation occurred at room temperature, *i.e.* 160–260 °C below the temperature required to initiate thermal reactions (R1) and (R2) and that the purity of H_2 was higher than in our TPD-MS experiment.

The trace gases, although in a small amount, showed a reach mass spectrum in the range of m/z 15–120, which was considerably different from the mass spectrum obtained under thermal desorption (see Fig. S2 in ESI‡). The components at m/z = 27–30, 55–60 and ≥84 in Fig. 2 can be assigned to alane and polyalanes (Al_xH_y, x = 1–4)[38] (see Table 1), which have not been found and reported under thermal desorption so far. The components at m/z = 50–54 might point to possible weak $NaAlH_4$ sublimation. The tentative assignment of other minor mass-spectrometric components is given in ESI.‡ These findings demonstrated that tribo-induced reactions must be significantly different from conventional thermal ones.

Further mechanistic insight into tribochemical processes can be gained through the analysis of mass-spectrometric time series, some of which are shown in Fig. 3. The analysis of emission dynamics, or behavioural analysis, is a useful tool for the interpretation of intrinsically non-stationary MSGE-MS signals, especially when a large uncertainty about the precursors composition exists.[29,32–34,39,40] It is based on a simple concept that if the mass-spectrometer signals arise from the same precursor their time series must show correlated behaviours. Then, the whole mass spectrum can be broken down into several groups in such a way that within each group signals

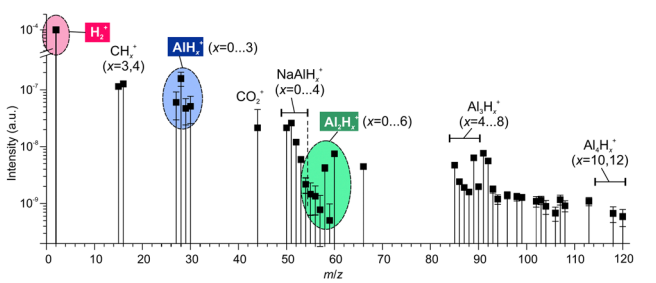

Fig. 2 The mass spectrum of gases emitted during rubbing of $NaAlH_4$. Hydrogen is the dominating species exceeding other components by 3 to 5 orders of magnitude.

Table 1 Assignments of possible ion species to their molecular precursors

m/z	Ions	H_2	AlH_3	Al_2H_6	$NaAlH_4$	Al_3H_9
2	H_2^+	•				
27	Al^+		•	•	•	•
28	AlH^+, CO^+		•	•	•	•
29, 30	AlH_x^+ (x=1,2)		•	•	•	•
50–53	$AlNaH_x^+$ (x=0-3)				•	
54	$AlNaH_4^+$, Al_2^+			•	•	
55-60	$Al_2H_x^+$ (x=1-6)			•		•
89, 90	$Al_3H_x^+$ (x=8,9)					•

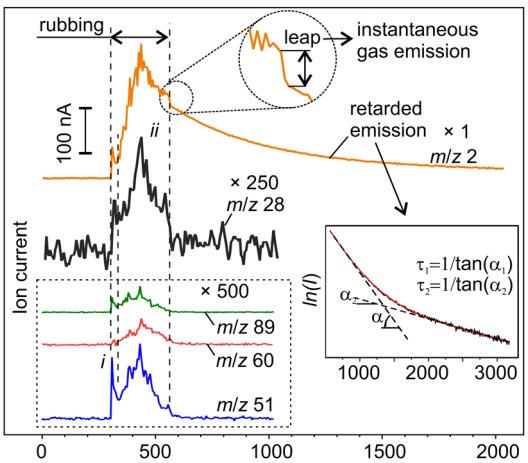

Fig. 3 The representative examples of mass-spectrometer time series. The signals other than m/z 2 are shown with large magnification. The inset shows the enlarged portion of the plot for m/z = 2 and the fit of the experimental data using linear functions on a semi-log scale.

are correlated. Then, each group can be analysed individually and independently from the rest, which significantly simplifies identifying the precursors. The second key concept relies on the fact that the complex emission dynamics is controlled by two processes: mechanical activation of new material volumes due to the expansion of the MAZ and the gas emission from mechanically affected material.[16,21] Therefore, the instantaneous emission rate can be described by a convolution of two functions: the rate of the MAZ expansion, R_v, and the specific rate of gas emission from a unit volume of activated material, q_s. The latter is a fundamental characteristic of the gas–solid system, which can be determined from the analysis of the gas pressure transients, while the R_v relies upon the severity of mechanical action and mechanical properties of the material and can be determined using structural and morphological analyses of mechanically affected zones.[21,33,41] These processes will be further analysed in Section 3.5.

At first sight, the emission behaviours of various gas components were quite similar and consisted of an initial peak (i) just at the beginning of rubbing and a series of irregular peaks superimposed on a slow varying base (ii) (Fig. 3). However, the proportions between the peaks and the base differed between the signals. More significant differences between the emission behaviours were found at and after the end of rubbing when all the signals except hydrogen returned to the background almost immediately. Some of them, *e.g.* m/z 60 and 89, tended to fade out even in the second half of stage ii before the end of rubbing. Such behaviour is typical for depleting emission sources.[34] The driving forces for such gas emission must be directly linked to mechanical action. In contrast, the emission of H_2 first leapt down to a certain non-zero value and then continued to decay for thousands of seconds forming a characteristic trail (Fig. 3).[21]

The synchronous emission, *i.e.* emission occurring during rubbing, and retarded emissions were analysed separately. Fig. 4 illustrates the analysis of correlations between various signals for synchronous emission, where a good example of a strong linear correlation (Pearson's r = 0.88–0.98) for the group of three alane ions AlH_x^+ (x = 0, 1 and 3) can be seen. The cross-correlation graph for m/z 27–28 shown in the inset in Fig. 4 is symmetric with respect to time lag 0, which means that both signals are correlated with no time lag. Surprisingly, the fourth

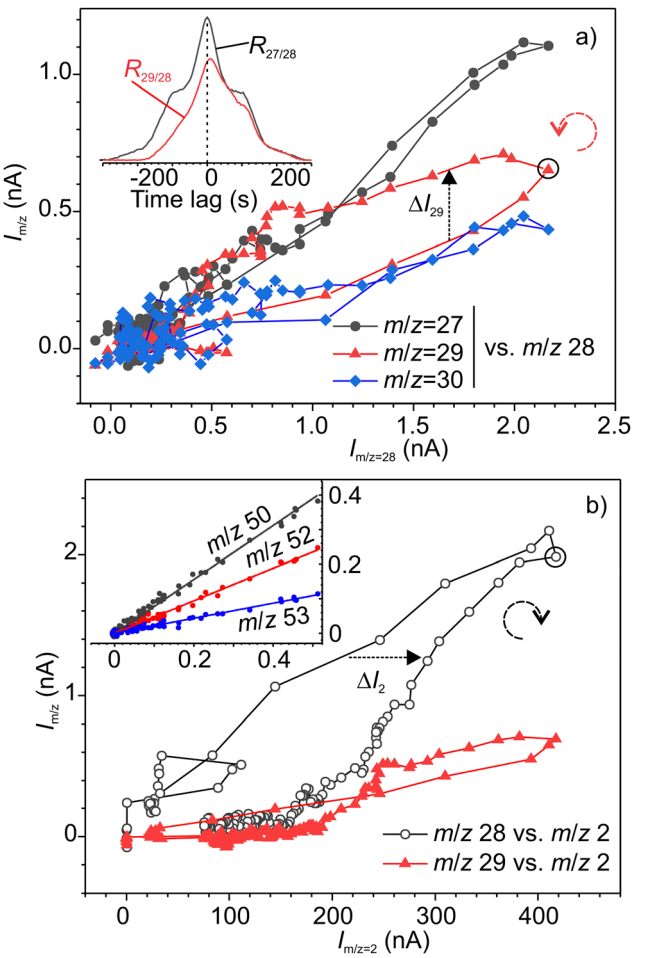

Fig. 4 Correlation analysis of mass-spectrometer signals: (a) m/z 27, 29 and 30 *vs.* m/z 28; (b) m/z 28 and 29 *vs.* m/z 2. The inset in (a) shows cross-correlation graphs for 27–28 and 29–27 signals. The inset in (b) shows the signals with m/z 50, 52 and 53 *vs.* m/z 51. The dashed arrows show the directions of the evolution of the signals with time in the corresponding loops.

ion of this group AlH_2^+ with m/z 29 exhibited a different, loop-like behaviour (Fig. 4a). The lack of linear correlation is also evident from the asymmetric shape of the cross-correlation graph for m/z 29–28 signals (inset in Fig. 4a). The maximum of this graph is positively shifted on around 10 s, indicating that the emission kinetics for the precursors of m/z 29 is slower or delayed with respect to the precursors of m/z 28. From the pair-wise analysis of signals m/z = 27–30 and m/z = 2 it was found that the signal m/z = 29 linearly correlated with hydrogen, but the rest of these ions did not (Fig. 4b). From the correlation of ions m/z = 29, 58, 59 and 60 (see Fig. 5 and Fig. S3 in ESI‡), we deduced that the second precursor must be dialane. The strongest linear correlations among the entire set of signals were found for the ions with m/z 50–53 (inset in Fig. 4b) which can undoubtedly be assigned to the only precursor – sodium alanate.

Based on the pairwise analysis, the correlations of all signals were classified into four types: strong and weak linear behaviours and strong and weak loop-like behaviours. Fig. 5 shows the map of pair-wise correlations. For some signals, which were denoted ''uncorrelated'', the dependency was not completely clear because of the data dispersion. The following major conclusions were drawn from the pairwise correlation analysis:

(a) there are notably strong correlations between the gases of group HAD (Hydrogen, Alane, Dialane). This means that H_2 must be formed simultaneously with mono- and di-alanes or that H_2 is a product of alanes decomposition.

(b) $NaAlH_4$ emission was not correlated with HAD which means that $NaAlH_4$ sublimation happened without its decomposition. We consider that sublimation should be related to the mechanical shearing of intermolecular bonds rather than to local frictional heating.

(c) Possible alkyl-substituted alanes ($AlH_2CH_3^+$) and/or CO_2^+ correlated with $NaAlH_4$, but not with HAD. The presence of methyl groups bonded to Al on the alanate surface, which was briefly exposed to the ambient air during introduction into the vacuum system, is not surprising since CO_2 can be reduced by alanates yielding methane.[42] However, such contamination must have only a minute effect on the dehydrogenation reaction since all these gases made up around 0.1% of the total emission yield.

(d) The emission of ions with higher masses could not be assuredly and uniquely ascribed to higher alanes. Contributions from other unidentified precursors are highly likely.

Further insight into hidden tribochemical processes was gained through the analysis of the retarded hydrogen emission. It is remarkable that the transient decays showed an unusual multistage behaviour, which could not be associated with one-step first-order tribodesorption processes such as those observed for MgH_2 and metals.[14,21,43] The time series could not be satisfactorily fitted using equations of reactions with order other than one (see ESI‡ for details). Thus, such reactions were discarded, and the analysis was focused on the interpretation of the trail emission as a combination of several first-order processes of different kinetics.[44] In fact, on a semi-logarithmic plot, the experimental data can be fitted reasonably well by a piece-wise linear function (inset in Fig. 3) including the fast (leap) and slow (tail) decays. A detailed analysis of gas emission dynamics and relevant underlying physical processes is given in Section 3.2.3. It can be advanced that the local temperature increase due to mechanical energy dissipation has been discarded as the possible driving force of H_2 emission.

3.2.2 Influence of load on the emission rate. When the test was repeated under varying normal loads the emission rates of all gases increased with the increasing load. The relative increase of the emission rates with loads was benchmarked against the mass spectrum measured at 0.44 N. Fig. 6a shows the mass spectra acquired under the loads 0.22, 0.88 and 1.32 N *vs.* the benchmark. All the data sets could be fitted reasonably well using a linear function with a unit slope. The mean relative increase of the emission rate under given loads was found as the antilogarithm of the intercepts of the fits to base 10. These data are plotted *vs.* applied load in Fig. 6b, which shows a clear deviation from a linear trend. For superficial tribochemical reactions, the reaction rate must vary with load, F, as $Q = kF^{\frac{2}{3}}$, where k is the proportionality coefficient, since the reaction rate is proportional to the contact area, which, in turn, is a $\frac{2}{3}$ power of the applied load (under elastic regime).[45] The red dashed line in Fig. 6b shows the least squares fit of the function $f = kF^{\frac{2}{3}}$ to the experimental data, which yielded a $R_{adj.}2$ = 0.6057. The inset of Fig. 6b shows the same data plotted *vs.* $F^{\frac{2}{3}}$, where a good linear dependency is evident. This finding confirms that the gas sources should be located at the sliding interface and in the mechanically affected bulk. The latter is a layer, several nanometeres to several micrometres thick, below the contact surface, where intensive plastic flow and structural degradation take place. The discussion on the effect of stress, strain, plastic flow and wear on gas emission will be continued in Section 3.4.

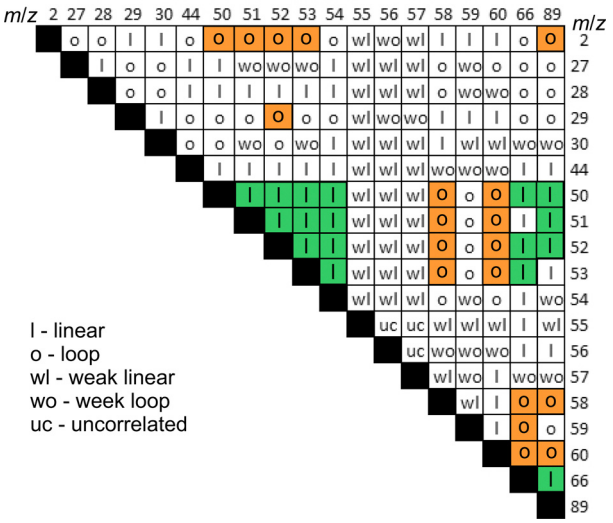

Fig. 5 Types of pairwise dependencies for mass-spectroscopic signals. Bold letters and the background highlight strong trends.

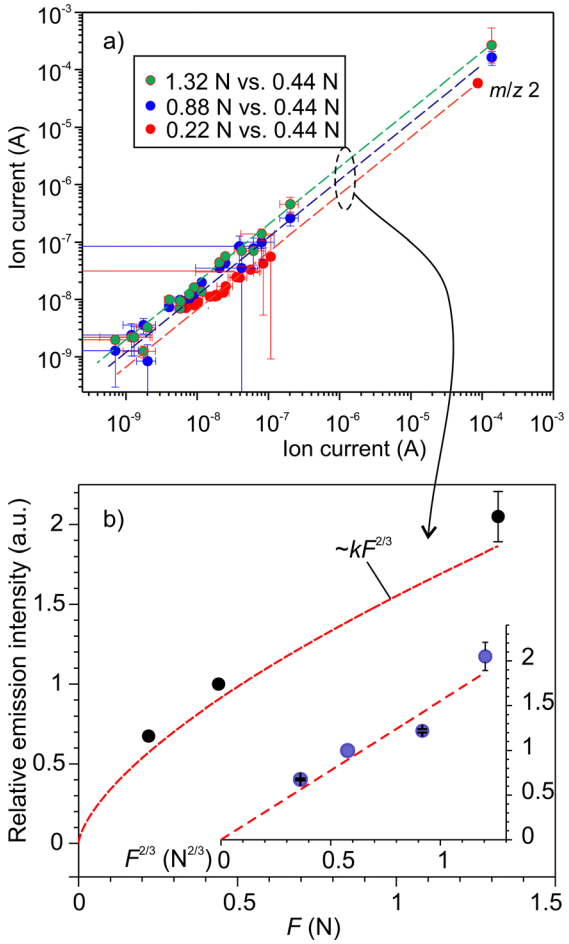

Fig. 6 (a) The effect of normal load on the emission intensity and the relative composition of emitted gases: (a) the mass-spectra (MS) obtained at the loads 0.22, 0.88 and 1.32 N *vs.* the MS at 0.44 N; (b) the relative increase of the emission rate as a function of normal load. The dashed line is the fit of the data using the function. $f = kF^{\frac{2}{3}}$. The inset shows the linear fit of the data as a function of $F^{\frac{2}{3}}$.

3.2.3 Quantification of hydrogen yield and analysis of emission dynamics. Considering that the trace gases constitute around 0.1% of the total emission rate, their contribution to the total emission rate can be neglected, and the emission can be considered a monocomponent one. Then, the emission rate can be quantified from the total pressure data using the following equation:[30,31]

$$Q = \frac{1}{I_e S S_0}\left(V\frac{d\Delta I}{dt} + C\Delta I(t)\right), \quad (1)$$

where I_e is the emission current of the ionization gauge, S_0 is the traceable calibrated sensitivity of the ionization gauge for N_2, S is the specific sensitivity to H_2, V is the volume of the vacuum chamber,[30] C is the diaphragm conductivity for H_2,[30] and ΔI is the increase of the ion current above the steady background.

Fig. 7a shows an example of time series of H_2 emission rate. In this graph, the oscillatory emission behaviour could be resolved (Fig. 7b) due to the higher data acquisition rate (50 samples s^{-1}). The frequency of the main mode of emission oscillation (1 Hz) perfectly matched the frequency of the indenters periodic motion (Fig. 7c). Further insight into the emission mechanisms was gained through a separate analysis of emission dynamics within each cycle and along various cycles. The falling edges in all cycles were fitted by real exponents using the Matrix Pencil Method[46] (see ESI‡ for details). The time constant obtained, τ_{s1}, is plotted in Fig. 8, which clearly shows an increasing trend. Also, during occasional emission bursts marked by arrows in Fig. 8, the time constant was anti-correlated with the total emission rate (Spearman correlation coefficient −0.439): the τ_{s1} increased when the Q_{H_2} decreased and *vice versa*. Furthermore, the decrease of τ_{s1} anticipated the appearance of the bursts. Such variations of gas emission dynamics cannot be connected to the fluctuations of surface temperature since heat dissipation at the interface was several orders of magnitude faster than the gas emission.§

The long-term emission dynamics can be characterized by the two parameters derived from the envelope curves shown by blue and green dashed lines in the inset in Fig. 7a. The lower envelope itself gives the offset, Q_2, while the difference between the upper and lower envelopes yields the oscillation amplitude, Q_1. Both these parameters depend on the decay kinetics.

To measure the emission decay parameters more accurately a separate test with a single rubbing stroke was done. In this case, H_2 rose more sharply and showed a bigger leap than after a multi-stroke test (Fig. 7e). The time constants of the three decay components are listed in Table 2, while the relative amplitudes were $A_1^s = 1.00$, $A_2^s = 0.0139$ and $A_3^s = 0.0111$, correspondingly. The τ_1^s was close to the value of τ_{s1} at the first strokes (Fig. 8) which corroborates our finding that the emission amplitude is controlled mainly by the fastest decay. In contrast, the τ_2^s and τ_3^s were significantly greater than the period of rubbing, and, therefore, they must control the slower dynamics of Q_2.

Assuming that to describe gas emission from spatially distributed sources, which are activated at different times, the additivity principle can be employed, the total instant gas flow can be expressed by the following equation:

$$Q(t) = \sum_{i=0}^{n-1} Q_{s,i}(t - i\Delta t), \quad (2)$$

where $Q(t)$ is the total gas flux after n rubbing cycles, $Q_{s,i}(t)$ is the flux generated in the i-th cycle, Δt is the period of rubbing, and t is the time. In our case $Q_{s,i}$ can be modelled by a sum of three real exponents:

$$Q_{s,i}(t - i\Delta t) = H(t - i\Delta t)\sum_{j=1}^{3} A_{j,i}\exp\left(-\frac{t - i\Delta t}{\tau_j^s}\right), \quad (3)$$

§ In Section 3.3 it is shown that the time constant of any emission decays is about three to five orders of magnitude larger than the time constant of heat dissipation at the interface.

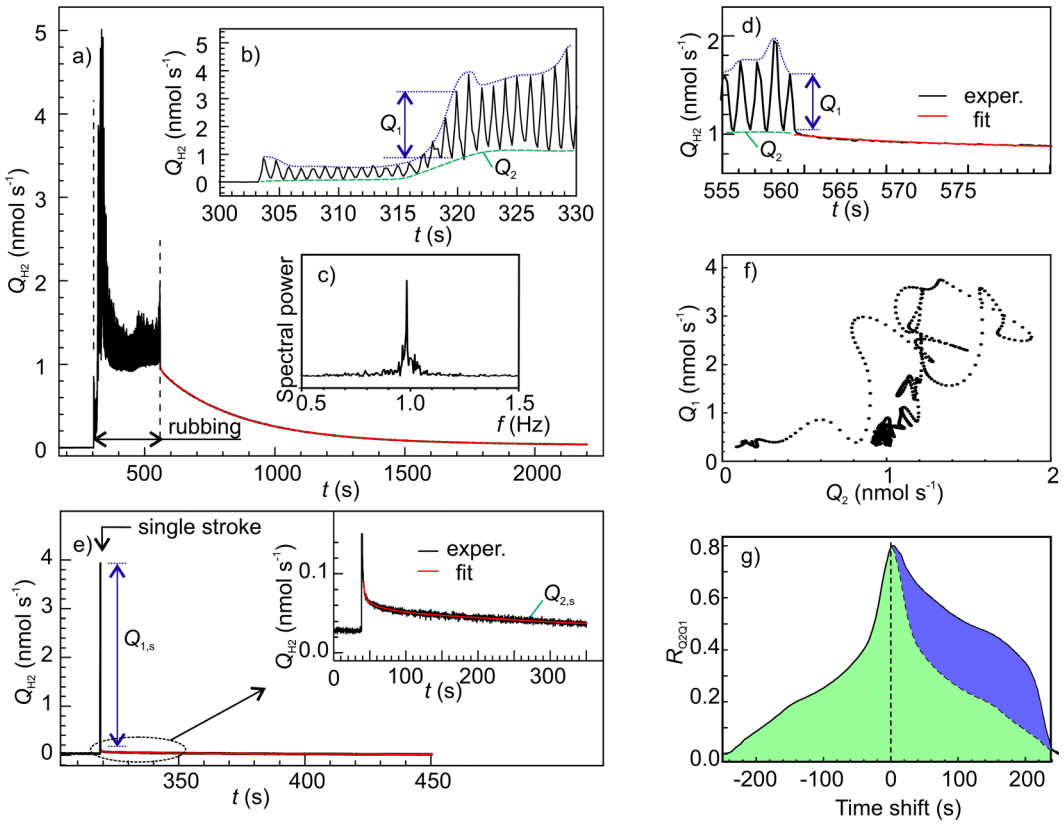

Fig. 7 (a) Time series of H_2 emission rate measured using an ion gauge; (b and d) the enlarged portions of the emission rate time series; (c) spectral power density of the emission rate oscillations; (e) gas emission response to a single rubbing stroke; (f) cross-dependencies between Q_1 and Q_2; (g) cross-correlation function of Q_2 concerning Q_1, the blue area denotes the portion of the graph, which deviates from symmetry.

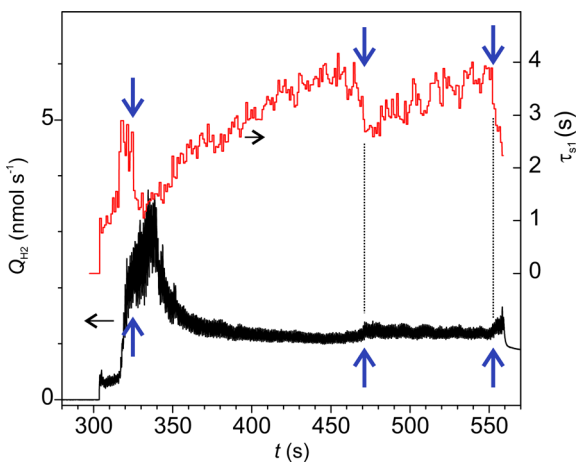

Fig. 8 The total H_2 emission rate and the characteristic time constant of transient decays during time lags between consecutive rubbing cycles. The arrows show the occasional events when the emission rate suddenly increased and the time constant decreased.

where $A_{j,i}$ are the pre-exponential factors of each decay component in i-th cycle, and H is Heaviside step function.

For the sake of simplicity, τ_1^s, which controls fast decay process, can be excluded from the expression for Q_2. Then

Table 2 The time constants (s) of exponentials fitted to the "trail" emission

Decay component		1	2	3
Multicycle: in-cycle	τ_{si}	0.77–4.2		
Multicycle: trail	τ_i^m		27.3	306
Single cycle	τ_i^s	0.638 ± 0.015	16.0 ± 0.452	465 ± 1.5

the following expression was obtained:

$$Q_2(t) = \sum_{j=2}^{3} \exp\left(-\frac{t}{\tau_j^s}\right) \sum_{i=0}^{n-1} A_{j,i} \exp\left(\frac{i\Delta t}{\tau_j^s}\right). \quad (4)$$

The summation of exponents does not affect the time constant of the resulting function, but its amplitude. Therefore, the parameters of exponential decay can be estimated from the retarded emission. Actually, the time constants in the "trail" after 500 rubbing cycles (Fig. 7) were $\tau_2^m = 27.2$ s and $\tau_2^m = 306$ s. These figures are not very different from the corresponding time constants in the single-stroke test. In contrast, the resulting amplitude in (4) increases with the number of cycles. Expression (4) also shows how Q_2 decreases with the gradual depletion of the emission sources during the test, which can be formally expressed as $A_{j,i} \geq A_{j,i+1}$. This tendency partially counteracts the increase of Q_2 with increasing τ_i^s. As a result, the Q_2 fluctuates around a certain constant value (Fig. 7 and 8).

The existence of three decay processes raises the question of whether they are interdependent or not. Fig. 7f shows the graph of Q_1 as a function of Q_2. It is surprising, that this graph does not display any random dispersion typical for experimental measurements, but presents a complex pattern, which resembles phase trajectories in the dynamical systems with chaos. This supports our hypothesis that all three decay processes probably stem from a single emission reaction. This was further corroborated by the cross-correlation analysis of Q_1 and Q_2 (Fig. 7g), which showed good correlation and a positive shift of Q_2, which means that Q_2 is delayed 20 to 220 s with respect to Q_1.¶ This time lag is within the time scale of τ_2^s and τ_3^s.

3.3 Surface characterization

The volume of mechanically affected material, V_{ma}, was estimated from the volume of worn material, V_w, which was determined from the cross-section profiles of the wear scars. A typical profile is shown in Fig. 9a. The maximal depth, d_w, width, $2a_w$, and the cross-section area, A_w, were measured at various points along the wear tracks and averaged.

The SEM image (Fig. 9b) shows the accumulation of fine agglomerated debris on both sides of the wear track. A closer look at the BSE-SEM images (Fig. 9c) did not reveal any significant grey shift indicating no major composition changes. The changes were mainly structural in form of longitudinal grooves on the worn surfaces and pile-ups on the sides. However, the network of deep cracks on the surface was not distorted by rubbing. This suggests that, under low and moderate load, material damage was localized at the contact zone, while its mechanisms were abrasion and plastic deformation. However, this does not preclude that under higher loads, the initial cracks could trigger the detachment of larger pieces of material, which could leave the contact zone without being crashed. This can explain why the amount of emitted hydrogen relatively decreased with increasing load. The enlarged portion of image 9c (Fig. 9i) revealed a number of submicrometer size debris.

Fig. 9d shows the total amount of emitted H_2 as a function of the normal load and the V_w. The molar efficiency of dehydrogenation, E_m, *i.e.* the number of moles of H_2obtained from one mole of deformed $NaAlH_4$, was estimated from the slope of the linear fit to the experimental data with zero intercepts. The apparent density of the cold-pressed pellets was about 1.4 g cm^{-3} [47] and the molar mass of $NaAlH_4$ is 54 g mol^{-1}. This yields E_m = 15% (see 2%), which is a fascinating result considering that the dehydrogenation took place at room temperature.

The absence of any noticeable chemical changes on the contact surfaces was confirmed by Raman spectrometry. Fig. 9e and f show the spectra which have the same characteristic bands assigned solely to $NaAlH_4$.[48–51] The only small difference between the two spectra concerns the decrease in intensity of the AlH_4^- libration mode at 432 cm^{-1}.

¶ The graph has an asymmetric shape. The blue highlighted shoulder on the right part shows the part of the graph, which diverges from symmetry. This shape indicates a correlation between Q_1 and Q_2 with a time lag, which matches the difference in time constant between fast and slow decay processes.

Such decrease and the red shift of libration band with increasing temperature were previously reported by Borgschulte *et al.*[52] This mode was associated with the external vibration of AlH_4^- as a rigid unit concerning a $NaAlH_4$ lattice.[53] Since in our study both spectra were measured at a constant temperature, the decrease of libration mode can be ascribed to the depletion of AlH_4^- concentration on the MAZ. Contrary to the expectations, the Na_3AlH_6 bands, which usually accompany thermal dehydrogenation, were not found. This result is also supported by micro-FTIR spectrometry (see Fig. S3 in ESI‡). According to these data, we can infer that triboinduced dehydrogenation of $NaAlH_4$ occurred through a chemical path, which is different from the sequential thermal reactions (R1) and (R2).

3.4 Frictional heat generation and a specific energy for hydrogen triboemission

The increase of contact temperature at sliding contact, ΔT, was modelled using Jaegers fundamental solution for moving heat sources.[48,49] Table 3 summarizes the parameters, which were fed into the model. Hardness, Young modulus and coefficient of friction (COF) were experimentally determined in this work. Fig. 10 shows the COF at various normal loads. COF was nearly constant during normal friction. The events of occasional recoverable damage at the surface were accompanied by temporal increases in COF. However, under higher loads, a transition from normal friction to high friction occurred when the density of defects achieved a critical level, which led to catastrophic damage to the material. The surface temperature was determined for both regimes.

Also, Jaegers model was used to determine the characteristic times of temperature flashes. The temperature maximum situated at the trailing part of the contact area because of large Pécklet numbers.[62,63] So, the duration of the temperature increase was approximately $t_c = 2a_w/V_s$, where V_s is the sliding velocity. For our experimental conditions t_c = 0.44–1.56 ms. The time constants of temperature decay of a surface point after leaving the contact zone were determined by fitting the dimensionless solution of Jaeggers equation at relevant Pécklet numbers. The resulting values ranged from 0.11 to 1.11 ms, which yielded the total duration of the temperature decay below 6 ms. It should be stressed that both heat-up and cool-down times are about three orders of magnitude smaller than the smallest empirically found time constant of H_2 triboemission. Bearing this in mind and taking into account that the maximal "flash" temperature was below 320 K, thermal effect of friction has been disregarded as a possible activation mechanism for $NaAlH_4$ dehydrogenation.

Although irrelevant for triggering tribochemical reactions, frictional heating is still an important channel of mechanical energy dissipation, together with the enthalpy of tribochemical reaction and the increment of internal energy of a solid. Taking into account that the mechanical energy equals the total work of friction, the following equation of energy balance can be written:

$$A_m = F_N N_c l_a \mu = \Delta H N_{H_2} + \Delta E + \Delta U \quad (5)$$

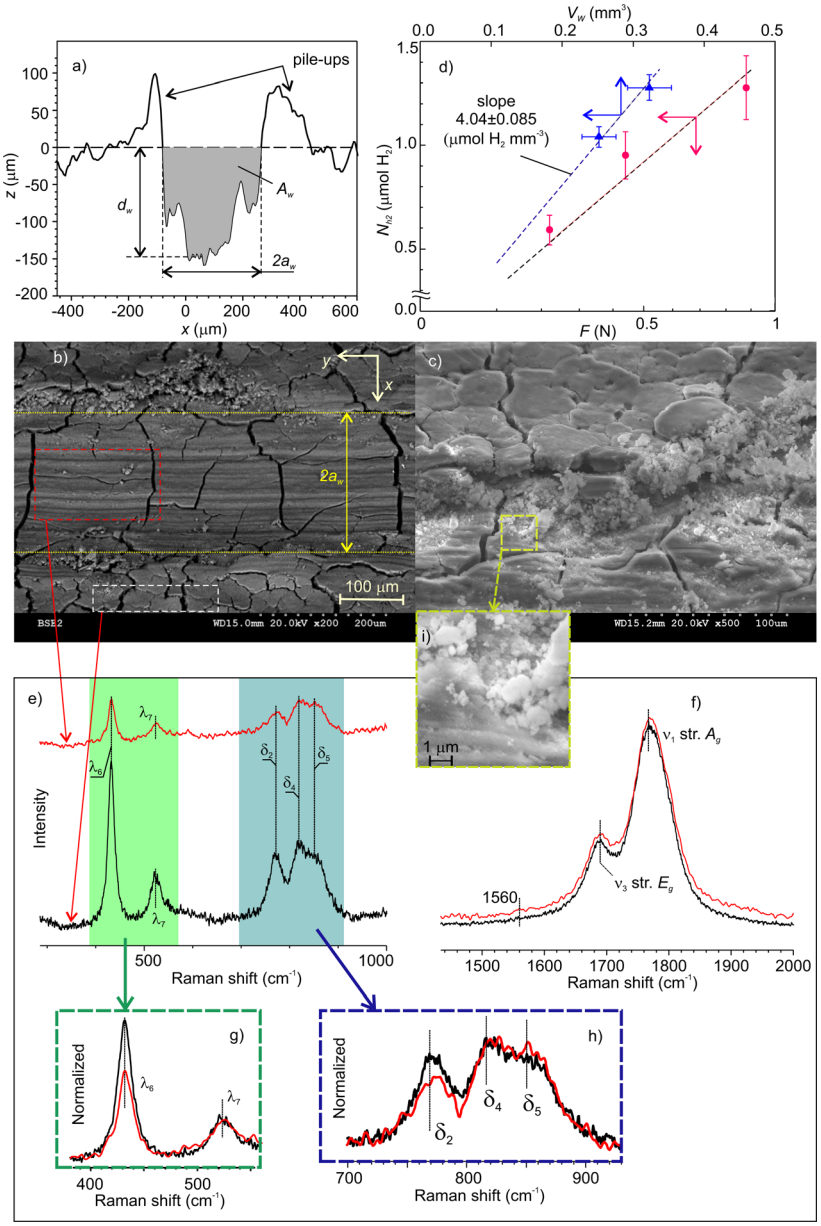

Fig. 9 (a) A cross-section of the wear track; (b and c) SEM images of the mechanically affected zones; (d) the total amount of emitted hydrogen as a function of the normal load and the volume of worn or displaced material; (e) low-frequency region of the Raman spectra of worn and pristine surface areas; (f) high-frequency region of the normalized Raman spectra of worn and pristine surface areas showing AlH_4^- libration mode; (g and h) the enlarged regions of the normalized low-frequency spectra shown in (e and i) enlarged portion of the image showing debris of sub-micrometer size.

where A_m is the work of friction force, F_N is the normal load, N_c is the number of rubbing cycles, l_a is the stroke, μ is the coefficient of friction, ΔH is the molar enthalpy of H_2 emission, ΔU is the increase of internal energy, ΔE is the thermal energy, and N_{H_2} is the number of moles of emitted H_2. The energy yield of tribochemical reaction was estimated as the number of moles of H_2 divided by the A_m:

$$W = \frac{N_{H_2}}{A_m}. \quad (6)$$

For F_n = 0.22–0.88 N and normal friction regime (Fig. 9b, green dots) the W varied between 2.8 and 4.5 mmol H_2 kJ^{-1}, which is notably higher than in many other mechanochemical reactions.[64] The energy spent for tribochemical emission of H_2 was estimated using the value for ΔH 40 kJ per mol H_2[10] and the values for N_{H_2} from Fig. 9d. This energy decreased from around 20% to 11% of the A_m as the normal load increased from 0.22 to 0.88 N. This finding corroborates our conclusion that frictional heating has nothing to do with the activation of tribochemical $NaAlH_4$ dehydrogenation since contact temperature increases with the normal load. By optimizing the way how the mechanical energy is applied and reducing the collateral energy burdens the energy yield of tribochemical reaction can be increased and the overall tribochemical dehydrogenation efficiency can be enhanced.

Table 3 Material parameters used for modelling the contact mechanics and the temperature at sliding contact

		$NaAlH_4$		
	Units	This study	Literature	Al_2O_3
Hardness	Mpa	0.7–0.9	5.77–9.17[54]	1800
Young modulus	Gpa	19–25	49.5–76.0[54] 51.8[57a]	345[55,56]
Poissons ratio			0.17–0.19[54,57]	0.23[56,58]
Thermal conductivity	W (m K)$^{-1}$		0.2[59] 0.2–1.6[47b] 0.28–0.55[61] 1.62–1.72[47]	34[60]
Density	kg m^{-3}		1240[47,59,61] 1380[47]	3780
Heat capacity	J (kg K)$^{-1}$		1584[59,61] 1150 ± 60[47]	784

Max. temperature increase ΔT (K)

	Load	
Friction regime	0.22 N	1.32 N
Normal	0.68	1.68
Catastrophic	3.77	9.39

[a] Calculated from the bulk modulus. [b] For pellets compacted at various pressures.

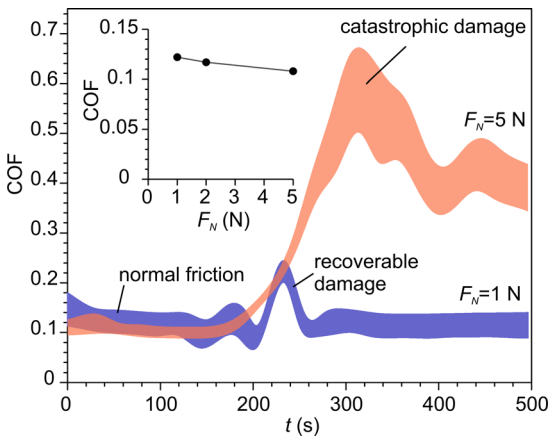

Fig. 10 The time series of coefficient of friction at various normal loads. Two regimes can be seen: normal friction and catastrophic damage. The inset shows the effect of the normal load on the normal COF.

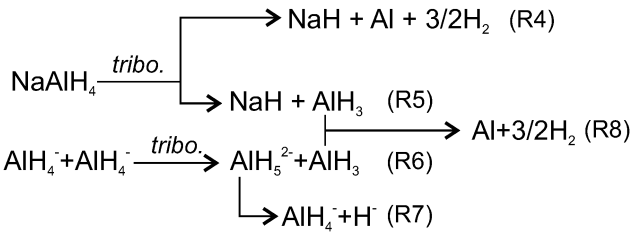

Fig. 11 Schematic reactions of tribo-induced dehydrogenation of $NaAlH_4$.

3.5 Possible mechanisms of non-thermal tribo-induced dehydrogenation of sodium alanate

This study led us to the conclusion that conventional two-step thermally driven reactions (R1) & (R2) cannot explain the tribochemical decomposition of $NaAlH_4$, since Na_3AlH_6 was not formed. Various authors[6,65] discussed the possibility that under specific conditions dehydrogenation of $NaAlH_4$ can go *via* alternative one-step (R4) or two-step ((R5) & (R8)) pathways (Fig. 11). For instance, when the size of $NaAlH_4$ nanoparticles is below 52 nm, reaction (R4) is thermodynamically more favourable than the conventional two-step reaction.[6] Baldé proposed that the activation energy decreases as the particle size decreases from 30 nm to below 10 nm.[65] Using these data and supposing that nanoparticles are produced by rubbing we found that the experimentally observed emission decays with time constants τ_1^s, τ_2^s and τ_3^s could be associated with the freshly generated nanoparticles of the following size: <2 nm, 2–10 nm and 10–19 nm, respectively (see ESI‡ for more details). However, generation of such a big number of ultra-fine nanoparticles (about 15% of the volume of MAZ) is questionable considering the mild rubbing conditions and the short duration of the test.[7]

The two-step pathway (R5) & (R8) does not seem plausible either. Although it can explain both H_2 and AlH_3 emission, the high energy barrier of the first step, *i.e.* separation of AlH_3 from AlH_4^- (enthalpy −60 kJ mol^{-1}[66] and activation energy 116 kJ mol^{-1}[67]) raises reasonable doubts about the effectiveness of mild mechanical forces to drive the reaction at room temperature. Effective coupling of the mechanical forces to an energy landscape of a chemical reaction usually takes place, when mechanical energy can be concentrated in a small volume, *i.e.* for hard and brittle materials. For soft materials such as $NaAlH_4$, the applied mechanical energy per bond constitutes only a minute fraction ($<0.05\%$) of the activation

barrier,[64,68–71] which is by far insufficient to drive hydrogen emission observed in this study.

Among various hypotheses, which can be put forward to explain the experimental findings, the following one appears to be the most plausible, although it still needs to be validated through additional atomic-scale studies and simulation. The hypothesis relies on the consideration of alternative ways of connecting mechanical energy and chemical reaction in materials of low hardness such as $NaAlH_4$ where various channels with low activation barriers for dissipation of mechanical energy can exist. Among others, the most energetically favourable microscopic mechanisms for mechanical energy dissipation include the generation and migration of vacancies, dislocations, crystal borders, twins and so on. These phenomena tend to increase structural disorder and entropy[36] that shifts the chemical potential of the solid and creates a thermodynamic force[72] leading to linked, but slipped in time, mass transport and chemical reactions.[73] On the atomic scale, the relative motion of atoms and atomic groups, which are only weakly bonded or not bonded under unstrained conditions, results in approaching each other and reaching the distances, at which chemical reactions between them become possible. Two of such possible reactions are shown in Fig. 11 ((R6) and (R7)). In the first step, the vertices of two AlH_4^- ions approach each other under applied stress. The nearest diagonally located AlH_4^- groups are likely to be involved. Then, H from one AlH_4 can be donated to another AlH_4 to form AlH_5^{2-}. The activation barrier of this reaction without external forces is only 32 kJ mol^{-1} H_2[74] and it requires a minute shift <1 Å of the Al atoms from their equilibrium positions.[75] Under spatial constraints induced by stress and strain the activation barrier can be further lowered.[76] The AlH_5^{2-} ion is metastable since the reverse barrier is about 4–10 kJ mol^{-1}.[77] It was reported that under elevated temperature, penta-coordinated Al could be further transformed to a hexa-coordinated state (energy barrier 36 kJ mol^{-1}), always when this transformation is accompanied by simultaneous diffusion of Na+ species to satisfy Coulomb neutrality and stabilize AlH_6^{3-} ions. However, under room temperature diffusion of AlH_3 and NaH vacancies is slow. For example, taking the value of diffusion activation barrier 44 kJ mol^{-1}[78,79] the diffusion rate at 295 K is more than two orders of magnitude lower, than at 400 K. Thus, the further transformation of AlH_5^{2-} into AlH_6^{3-} is kinetically hindered, and decomposition of AlH_5^{2-} proceeds according to (R7). This hypothesis agrees with our experimental findings, *i.e.* lack of Raman bands of Na_3AlH_6 and the decrease of libration Raman mode due to consumption of AlH_4^- groups in reactions (R6) and (R7).

Further formation of H_2 can proceed through the association of two hydrides (R7) or *via* the decomposition of alane (R6). Reaction (R8) shows the formation of H_2 from alane, which should occur in the bulk since alane is relatively stable in the gas phase.[4] Alanes must be formed at or very close to the interface where neutral AlH_3 is more favoured than other ionic species since electrostatic caging by Na^+ is less perfect than in the bulk.[75] In addition, slow diffusion of alane at room temperature should hinder their release from deeper layers in a reasonable time. Concerning H^-, despite the fact that two hydride ions cannot meet each other directly due to strong Coulomb repulsion, the formation of H_2 can proceed through various intermediate steps, which were previously investigated.[66,75,77,80–82] H^- can easily diffuse from the bulk to the surface through minute rotation and rebinding of neighbouring tetrahedral[67] whose free-energy barrier for diffusion is 11.6–15.4 kJ mol^{-1}.[78,81] Such a low energy barrier makes diffusion much less sensitive to temperature decrease, than diffusion of metal species. At 295 K the rate of H^- diffusion is only 3.6-fold lower, than at 400 K. Therefore, at 295 K H diffusion becomes the dominating process controlling the overall reaction rate. In contrast, diffusion of molecular hydrogen in $NaAlH_4$, which occurs as migration of interstitial defect (free-energy barrier around 24 kJ mol^{-1})[78] is too slow at room temperature to match any observed H_2 emission decays. Thus, the emitted H_2 must be formed at the surface or in a thin (few nanometers) subsurface layer, where intensive mixing of atoms and gas diffusion take place.[83]

3.6 Emission kinetics and its relationship with the expansion of mechanically affected zone

The model of one-side diffusion from a layer was employed to estimate the thickness of the layer contributing to mechanically stimulated H_2 emission (Fig. 12a).[84] The layer thickness is related to the time constant of the emission decay, τ_D, by the following expression:

$$d_w = \frac{\pi}{2}\sqrt{D\tau_D} \quad (7)$$

where D is the diffusion coefficient. The value of D was estimated from neutron scattering data reported by Shi *et al.*[85] assuming that the activation barrier is 12.0–29.9 kJ mol^{-1}. It yielded D = (2.5–13) $\times$ 10^{-7} cm^2 per s at 300 K. Then, substituting the τ_D by the empirical time constants τ_i^s, (i = 1, 2, 3) we obtained: d_{w1} = 5–15 μm, d_{w2} = 30–70 μm and d_{w3} = 150–400 μm. These values should be considered as upper limits since a recombination step, which can limit the overall emission rate, was not included in the model. These figures are consistent with the thickness of the deformed layer, which can be assessed from microscopy images shown in Fig. 9a as well as with the Hertz model. The topmost layer of thickness d_{w1} must be responsible for the fastest and most intensive emission component. The d_{w1} coincides with the thickness of the plastically deformed layer on the MAZ, which spans from the surface to the depth $0.47a_w$, where a_w = 20–36 μm depending on the applied load. At this depth, the stress reaches the maximum. A deeper layer between 31 and 71 μm from the surface, which is subjected to less intensive shear stress, must contribute to the slower emission with time constants 16–27 s. Finally, very deep zones situating below 100 μm must be responsible for the slowest emission component and can be activated due to stress concentrations at the grain boundaries and other defects, which are abundant in such an irregular material as compacted pellets. The diffusion model consistently

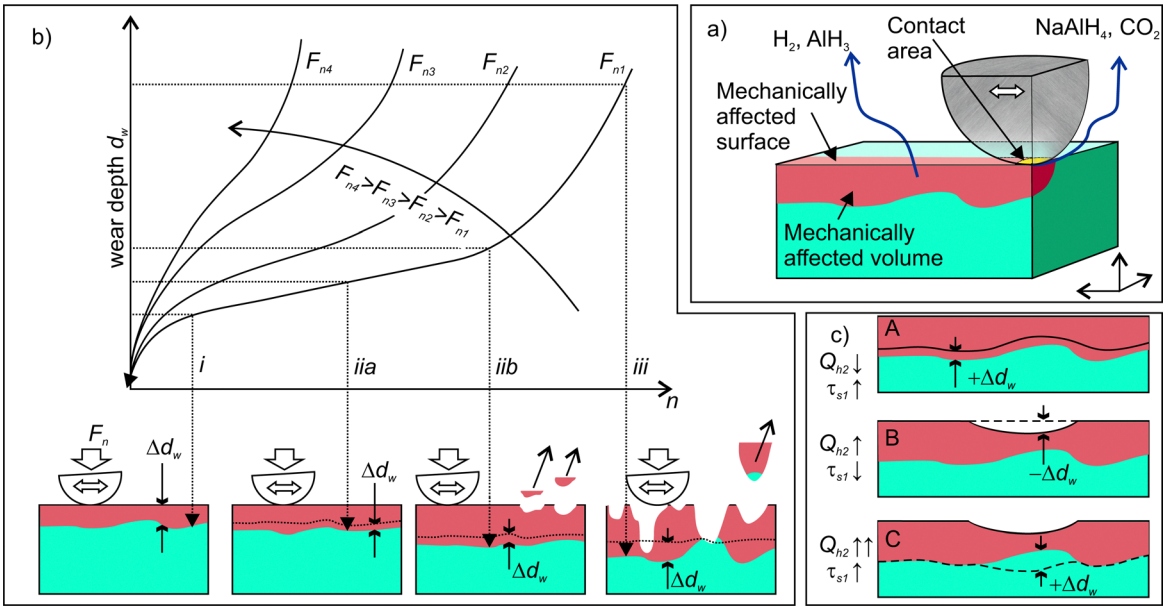

Fig. 12 (a) Schematic drawing of the main sources of gas emission; (b) schematic drawing explaining the expansion of the volume of the mechanically affected zone with the number of cycles (n) and under various normal loads (F_n). Three different regimes are shown: (i) – initial fast expansion during the run-in and mutual adaptation of mating surfaces, (ii)-steady expansion of the volume of the mechanically affected zone. This stage can involve the detachment of wear particles (iib) or not (iia). The wear particles originate from intensively deformed surface zones mainly. (iii) – intensive or "catastrophic" wear, which initiates when the concentration of internal defect has reached a critical level. A larger volume of wear particles is generated, and the particles can be detached from both deformed and pristine zones. (c) Schematic drawing illustrating the correlated variations of the rate of H_2 emission and the time constant.

explains the correlated behaviour of the emission amplitude and the offset (Fig. 7f and g) as well as the variations of emission kinetics with time and its correlation with the emission intensity (Fig. 8).

The results of this study demonstrated the crucial role of stress and strain for tribo-induced dehydrogenation of $NaAlH_4$. The connection between the structural degradation (deformation propagation and material damage) in the contact zone and the dynamics of gas emission has been further analysed using the well-established kinetic model of wear, which is schematically shown in Fig. 12b. At the beginning of rubbing, high contact stress causes intensive material deformation (stage (i) in Fig. 12) that can be associated with the emission bursts (stage (i) in Fig. 3). After several tens of rubbing cycles, the contact area increases, while the contact stress decreases. This leads to the stabilization of the wear rate at a lower value. At this stage, the same material is repeatedly deformed each cycle causing a gradual depletion of the emission sources. Occasional local damages and detachments of microscopic debris from the contact zone (iib in Fig. 12a) can intensify the propagation of deformation into a deeper fresh layer[86] giving rise to the emission bursts of low intensity at stage (ii) (Fig. 3). When a critical density of defects in the deformed layer is attained, gradual wear switches to a catastrophic one, and fast material disintegration begins. This is accompanied by intensive but chaotic emission behaviour. When the applied load increases the duration of the second stage decreases, as shown by arrows in Fig. 12b.

Furthermore, the linked diffusion-wear model put forward in this work can consistently explain the variations of the time constants of H_2 emission, τ_{s1}, from the perspective of the dynamics of the thickness of the deformed layer, d_w. The gradual increase of the τ_{s1} from 1 to 4 s (Fig. 8) must be associated with the about the two-fold increase of the d_w (scheme A in Fig. 12c). The emission bursts and the corresponding sharp drops of τ_{s1} can be explained by a sudden decrease of the d_w at the spots, where the material was locally damaged and removed (scheme B in Fig. 12c). This could trigger further propagation of deformation into the bulk and involvement of new material volumes in the mechanically affected zone.

4 Conclusions

Intensive instantaneous dehydrogenation of undoped $NaAlH_4$ was achieved at room temperature using mechanical energy *via* rubbing in vacuum. H_2 was the main emitted species constituting >99% of the total emission. Among minor components, alanes, dialanes, CO_2 and traces of $NaAlH_4$ were identified. Behavioural analysis of the pressure time series showed that emissions of H_2, alanes and dialanes were highly correlated. This was ascribed to the fact that these gases originated from the same chemical reactions.

Further analysis of the H_2 emission flux at higher time resolution revealed that the emission decay consisted of two

events: the fast decay lasting for a few seconds and a slow retarded emission having various decay components and lasting for thousands of seconds after the end of rubbing. This suggests that the sources of H_2 emission must be situated both in the mechanically affected bulk and on the surface of the contact zone. The molar efficiency of dehydrogenation under given experimental conditions was $\geq$15% (mol H_2 per mol $NaAlH_4$).

Various possible emission mechanisms lying behind tribo-induced emission were scrutinized. The thermal effect of friction and the direct coupling of mechanical forces to the energy landscape of chemical reactions were ruled out. An alternative reaction pathway based on the idea that chemical reactions were triggered by the activation of various channels of mechanical energy dissipation in the solid, was proposed. It suggests that the activation barrier for the reaction between unbound or weakly bound groups can be lowered during their mutual approach under strain. On this ground, a linked diffusion-wear model of tribo-induced dehydrogenation of $NaAlH_4$ was proposed. It consistently explains all empirical findings including the complex dynamics of emission time series, the kinetics of emission decays and their relationship with the degree of wear.

Author contributions

E. M.-C.: methodology, validation, formal analysis, investigation. A. G.: formal analysis. O. I.: software, investigation. M. M. S., B. Z., E. F.: investigation. J. R. A., R. N.: conceptualization, methodology, validation, formal analysis, investigation, writing, funding acquisition, supervision, project administration.

Conflicts of interest

There are no conflicts to declare.

Acknowledgements

We acknowledge E. Roman, G. Moras, S. Sukhomlinov and M. Boiko for fruitful discussion and L. García-Pelayo for assistance with ultra microindentation experiments. MIRE Group thanks to F. Moreno and M. López del Campo for their technical assistance. This work was financially supported by the Ministry of Science and Innovation of Spain (grants PID2019-111063 RB-I00, PID2020-112770RB-C22, RTI2018-099794-B-I00, and TED2021-129950B-I00) and the Basque Government *via* the EMAITEK Plus 2020 programme.

Notes and references

1 B. Bogdanovic, R. A. Brand, A. Marjanovi, M. Schwickardi and J. Tölle, *J. Alloys Compd.*, 2000, **302**, 36–58.
2 S.-i Orimo, Y. Nakamori, J. R. Eliseo, A. Züttel and C. M. Jensen, *Chem. Rev.*, 2007, **107**, 4111–4132.
3 B. Bogdanovic and M. Schwickardi, *J. Alloys Compd.*, 1997, **253–254**, 1–9.
4 S. Chaudhuri, J. Graetz, A. Ignatov, J. J. Reilly and J. T. Muckerman, *J. Am. Chem. Soc.*, 2006, **128**, 11404–11415.
5 F. Schüth, B. Bogdanovic and M. Felderhoff, *Chem. Commun.*, 2004, 2249–2258.
6 T. Mueller and G. Ceder, *ACS Nano*, 2010, **4**, 5647–5656.
7 J. R. Ares, K. F. Aguey-Zinsou, M. Porcu, J. M. Sykes, M. Dornheim, T. Klassen and R. Bormann, *Mater. Res. Bull.*, 2008, **43**, 1263–1275.
8 V. Stavila, R. K. Bhakta, T. M. Alam, E. H. Majzoub and M. D. Allendorf, *ACS Nano*, 2012, **6**, 9807–9817.
9 Y. Li, G. Zhou, F. Fang, X. Yu, Q. Zhang, L. Ouyang, M. Zhu and D. Sun, *Acta Mater.*, 2011, **59**, 1829–1838.
10 R. K. Bhakta, S. Maharrey, V. Stavila, A. Highley, T. Alam, E. Majzoub and M. Allendorf, *Phys. Chem. Chem. Phys.*, 2012, **14**, 8160–8169.
11 C. P. Baldé, B. P. C. Hereijgers, J. H. Bitter and K. P. de Jong, *Angew. Chem., Int. Ed.*, 2006, **45**, 3501–3503.
12 D. Pukazhselvan, B. K. Gupta, A. Srivastava and O. N. Srivastava, *J. Alloys Compd.*, 2005, **403**, 312–317.
13 J.-R. Ares, R. Nevshupa, E. Muñoz-Cortés, C. Sánchez, F. Leardini, I.-J. Ferrer, V. Minh Huy Tran, F. Aguey-Zinsou and J.-F. Fernández, *ChemPhysChem*, 2019, **20**, 1248–1262.
14 R. Nevshupa, J. R. Ares, J. F. Fernandez, A. del Campo and E. Roman, *J. Phys. Chem. Lett.*, 2015, **6**, 2780–2785.
15 R. Nevshupa and K. Hiratsuka, in *Triboluminescence*, ed. E. Gnecco and E. Meyer, Springer International Publishing, 2015, book section 4, pp. 57–77.
16 R. Nevshupa, *J. Frict. Wear.*, 2009, **30**, 118–126.
17 V. V. Boldyrev, *Russ. Chem. Rev.*, 2006, **75**, 177–190.
18 K.-F. Aguey-Zinsou and J.-R. Ares-Fernandez, *Energy Environ. Sci.*, 2010, **3**, 526–543.
19 A. Porcheddu, A. Cincotti and F. Delogu, *Int. J. Hydrogen Energy*, 2021, **46**, 967–973.
20 R. A. Nevshupa, E. Roman and J. L. de Segovia, *Int. J. Mater. Prod. Technol.*, 2010, **38**, 57–65.
21 R. Nevshupa, K. Cruz, I. Martinez, S. Ramos, I. Llorente and E. Roman, *Tribol. Int.*, 2016, **97**, 360–370.
22 *Exo-electron Emission and Tribochemistry*, ed. Q. J. Wang and Y.-W. Chung, Springer US, Boston, MA, 2013, p. 998.
23 J. Zhang, Y. C. Zhou, Z. S. Ma, L. Q. Sun and P. Peng, *Int. J. Hydrogen Energy*, 2013, **38**, 3661–3669.
24 K. Nogita, X. Q. Tran, T. Yamamoto, E. Tanaka, S. D. McDonald, C. M. Gourlay, K. Yasuda and S. Matsumura, *Sci. Rep.*, 2015, **5**, 8450.
25 J. Huot, G. Liang and R. Schulz, *J. Alloys Compd.*, 2003, **353**, L12–L15.
26 K. Suárez-Alcántara, J. R. Tena-Garcia and R. Guerrero-Ortiz, *Materials*, 2019, **12**, 2724.
27 Y. Shang, C. Pistidda, C. Milanese, A. Girella, A. Schökel, T. T. Le, A. Hagenah, O. Metz, T. Klassen and M. Dornheim, *Green Chem.*, 2022, **24**, 4153–4163.
28 A. Rusanov, R. Nevshupa, J. M. Martin, M. A. Garrido and E. Roman, *Diamond Relat. Mater.*, 2015, **55**, 32–40.

29 R. Nevshupa, J. Caro, A. Arratibel, R. Bonet, A. Rusanov, J. R. Ares and E. Roman, *Tribol. Int.*, 2019, **129**, 177–190.
30 R. A. Nevchoupa, J. L. de Segovia and E. A. Deulin, *Vacuum*, 1999, **52**, 73–81.
31 R. A. Nevshupa, M. Conte, A. Igartua, E. Roman and J. Luis de Segovia, *Tribol. Int.*, 2015, **86**, 28–35.
32 M. Mahrova, M. Conte, E. Roman and R. Nevshupa, *J. Phys. Chem. C*, 2014, **118**, 22544–22552.
33 A. Rusanov, R. Nevshupa, J. Fontaine, J.-M. Martin, T. Le Mogne, V. Elinson, A. Lyamin and E. Roman, *Carbon*, 2015, **81**, 788–799.
34 R. Nevshupa, M. Conte, S. Guerra and E. Roman, *Lubricants*, 2017, **5**, 27.
35 W. C. Oliver and G. M. Pharr, *J. Mater. Res.*, 1992, **7**, 1564–1583.
36 M. Christian and K.-F. Aguey-Zinsou, *Nanoscale*, 2010, **2**, 2587–2590.
37 A. V. Phelps, *J. Phys. Chem. Ref. Data*, 1992, **21**, 883–897.
38 C. P. Nold and J. D. Head, *J. Phys. Chem. A*, 2012, **116**, 4348–4355.
39 R. Nevshupa, M. Conte, A. del Campo and E. Roman, *Tribol. Int.*, 2016, **102**, 19–27.
40 S. Mori, T. Kawada and W. C. Xu, *Appl. Surf. Sci.*, 1997, **108**, 391–397.
41 A. Igartua, E. Berriozabal, R. Nevshupa, E. Roman, F. Pagano, L. P. Nielsen, S. Louring and L. Muntada, *Tribol. Int.*, 2017, **114**, 192–200.
42 C. L. Hugelshofer, A. Borgschulte, E. Callini, S. K. Matam, J. Gehrig, D. T. Hog and A. Züttel, *J. Phys. Chem. C*, 2014, **118**, 15940–15945.
43 C. R. Bagshaw, in *Transient-State Kinetic Methods*, ed. G. C. K. Roberts, Springer Berlin Heidelberg, Berlin, Heidelberg, 2013, pp. 2638–2644.
44 T. Jacobs, C. M. Mate, K. Turner and R. Carpick, *Scanning Probe Microscopy for Industrial Applications: Nanomechanical Characterization*, 2013, p. 368.
45 V. N. Ageev, E. Y. Zandberg, N. I. Ionov and A. Y. Tontegode, *Phys.-Usp.*, 1983, **26**, 382–383.
46 M. Henry, O. Ibryaeva, D. Salov and A. Semenov, Bulletin of the South Ural State University. Series ''Mathematical Modelling, Programming and Computer Software'', 2017, 10, 92–104.
47 B. A. van Hassel, D. Mosher, J. M. Pasini, M. Gorbounov, J. Holowczak, X. Tang, R. Brown, B. Laube and L. Pryor, *Int. J. Hydrogen Energy*, 2012, **37**, 2756–2766.
48 D. J. Ross, M. D. Halls, A. G. Nazri and R. F. Aroca, *Chem. Phys. Lett.*, 2004, **388**, 430–435.
49 S. Gomes, G. Renaudin, H. Hagemann, K. Yvon, M. P. Sulic and C. M. Jensen, *J. Alloys Compd.*, 2005, **390**, 305–313.
50 T. G. Adiks, V. V. Gavrilenko, L. I. Zakharkin and L. A. Ignat'eva, *J. Appl. Spectrosc.*, 1967, **6**, 546–551.
51 M. Enders, M. Kleber, G. Derscheid, K. Hofmann, H.-D. Bauer and B. Scheppat, *Appl. Opt.*, 2020, **59**, 9510–9519.
52 A. Borgschulte, A. Züttel, P. Hug, G. Barkhordarian, N. Eigen, M. Dornheim, R. Bormann and A. J. Ramirez-Cuesta, *Phys. Chem. Chem. Phys.*, 2008, **10**, 4045–4055.
53 H. Yukawa, N. Morisaku, Y. Li, K. Komiya, R. Rong, Y. Shinzato, R. Sekine and M. Morinaga, *J. Alloys Compd.*, 2007, **446–447**, 242–247.
54 R.-K. Pan, J.-G. Yao, R.-L. Ji, W.-W. Liu and D.-F. Yin, *Int. J. Hydrogen Energy*, 2018, **43**, 3862–3870.
55 C. Baudín, in *Alumina, Structure and Properties*, ed. M. Pomeroy, Elsevier, Oxford, 2021, pp. 25–46.
56 M. Asmani, C. Kermel, A. Leriche and M. Ourak, *J. Eur. Ceram. Soc.*, 2001, **21**, 1081–1086.
57 L. George and S. K. Saxena, *Int. J. Hydrogen Energy*, 2010, **35**, 5454–5470.
58 P. Auerkary, *Mechanical and physical properties of engineering Alumina ceramics, Technical notes*, Julkaisija-Utgivare, Technical research center of Finland, Espoo, 1996.
59 B. Bonnetot, G. Chahine, P. Claudy, M. Diot and J. M. Letoffe, *J. Chem. Thermodyn.*, 1980, **12**, 249–254.
60 M. Kobayashi, T. Goto, T. Aoba and H. Miura, *Mater. Charact.*, 2019, **154**, 424–436.
61 D. E. Dedrick, M. P. Kanouff, B. C. Replogle and K. J. Gross, *J. Alloys Compd.*, 2005, **389**, 299–305.
62 X. Tian and J. F. E. Kennedy, *J. Tribol.*, 1994, **116**, 167–174.
63 F. E. Kennedy, in *Frictional heating and contact temperatures*, ed. B. Bhushan, Taylor & Francis, 2010, pp. 235–272.
64 P. Y. Butyagin and I. K. Pavlichev, *React. Solids*, 1986, **1**, 361–372.
65 C. Baldé, *Sodium alanate nanoparticles for hydrogen storage*, PhD thesis, Utrecht University, Utrecht, 2008, p. 101.
66 W. Grochala and P. P. Edwards, *Chem. Rev.*, 2004, **104**, 1283–1316.
67 H. Gunaydin, K. N. Houk and V. Ozolinš, *Proc. Natl. Acad. Sci. U. S. A.*, 2008, **105**, 3673–3677.
68 J. Li, C. Nagamani and J. S. Moore, *Acc. Chem. Res.*, 2015, **48**, 2181–2190.
69 A. E. M. Beedle, M. Mora, C. T. Davis, A. P. Snijders, G. Stirnemann and S. Garcia-Manyes, *Nat. Commun.*, 2018, **9**, 3155.
70 A. J. Walton, *Adv. Phys.*, 1977, **26**, 887–948.
71 K. Nakayama and R. A. Nevshupa, *Vacuum*, 2004, **74**, 11–17.
72 H. Qian, S. Kjelstrup, A. B. Kolomeisky and D. Bedeaux, *J. Phys.: Condens. Matter*, 2016, **28**, 153004.
73 B. E. Klamecki, *Wear*, 1984, **96**, 319–329.
74 G. K. P. Dathar and D. S. Mainardi, *J. Phys. Chem. C*, 2010, **114**, 8026–8031.
75 F. Sterpone, S. Bonella and S. Meloni, *J. Phys. Chem. C*, 2012, **116**, 19636–19643.
76 C. L. Carr, W. Jayawardana, H. Zou, J. L. White, F. El Gabaly, M. S. Conradi, V. Stavila, M. D. Allendorf and E. H. Majzoub, *Chem. Mater.*, 2018, **30**, 2930–2938.
77 F. Zhang, B. C. Wood, Y. Wang, C.-Z. Wang, K.-M. Ho and M.-Y. Chou, *J. Phys. Chem. C*, 2014, **118**, 18356–18361.
78 G. B. Wilson-Short, A. Janotti, K. Hoang, A. Peles and C. G. Van de Walle, *Phys. Rev. B: Condens. Matter Mater. Phys.*, 2009, **80**, 224102.
79 K. J. Michel and V. Ozolinš, *J. Mater. Chem. A*, 2014, **2**, 4438–4448.

80 M. Felderhoff and B. Zibrowius, *Phys. Chem. Chem. Phys.*, 2011, **13**, 17234–17241.
81 M. Monteferrante, S. Bonella, S. Meloni, E. Vanden-Eijnden and G. Ciccotti, *Scientific Modeling and Simulation SMNS*, 2008, **15**, 187–206.
82 E. G. Sorte, R. C. Bowman, E. H. Majzoub, M. H. W. Verkuijlen, T. J. Udovic and M. S. Conradi, *J. Phys. Chem. C*, 2013, **117**, 8105–8113.
83 E. A. Deulin and R. A. Nevshupa, *Appl. Surf. Sci.*, 1999, **144–145**, 283–286.
84 J. Crank and E. Crank, *The Mathematics of Diffusion*, Clarendon Press, 1979.
85 Q. Shi, J. Voss, H. S. Jacobsen, K. Lefmann, M. Zamponi and T. Vegge, *J. Alloys Compd.*, 2007, **446–447**, 469–473.
86 S. B. Bulgarevich, M. V. Boiko and V. A. Feizova, *J. Frict. Wear*, 2017, **38**, 316–320.

